

Strong Release of Methane on Mars in Northern Summer 2003

Michael J. Mumma,^{1*} Geronimo L. Villanueva,^{2,3} Robert E. Novak,⁴
Tilak Hewagama,^{3,5} Boncho P. Bonev,^{2,3} Michael A. DiSanti,³
Avi M. Mandell,³ Michael D. Smith³

¹NASA Goddard Space Flight Center, Mailstop 690.3, Greenbelt, MD 20771, USA.

²Department of Physics, Catholic University of America, Washington DC, 20008 USA.

³NASA Goddard Space Flight Center, Mailstop 693, Greenbelt, MD 20771, USA.

⁴Department of Physics, Iona College, New Rochelle, NY 10801, USA.

⁵Department of Astronomy, University of Maryland, College Park, MD 20742-2421, USA.

*To whom correspondence should be addressed. E-mail: michael.j.mumma@nasa.gov

Abstract

Living systems produce more than 90% of Earth's atmospheric methane; the balance is of geochemical origin. On Mars, methane could be a signature of either origin. Using high-dispersion infrared spectrometers at three ground-based telescopes, we measured methane and water vapor simultaneously on Mars over several longitude intervals in (northern) early- and late-summer 2003 and near vernal equinox 2006. When present, methane occurred in extended plumes and the maxima of latitudinal profiles imply that the methane was released from discrete regions. At northern mid-summer, the principal plume contained ~19,000 metric tons of methane and the estimated source strength ($\geq 0.6 \text{ kg s}^{-1}$) was comparable to that of the massive hydrocarbon seep at Coal Oil Point (Santa Barbara, CA).

The atmosphere of Mars is strongly oxidized, composed primarily of carbon dioxide (CO₂, 95.3%) along with minor nitrogen (N₂, 2.7%), carbon monoxide (CO, 0.07%), oxygen (O₂, 0.13%), water vapor (H₂O, 0–300 ppm), and radiogenic argon (1.6%); other species and reduced gases such as methane (CH₄) are rare. CH₄ production by atmospheric chemistry is negligible and its lifetime against removal by photochemistry is estimated to be several hundred years (1-3) or shorter if strong oxidants such as peroxides are present in the surface or on airborne dust grains (4). Thus, the presence of significant methane would require recent release from sub-surface reservoirs; the ultimate origin of this methane is uncertain, but it could be either abiotic or biotic (2,5,6).

Before 2003, all searches for methane were negative (7-9). Since then, three groups have reported detections of methane (10-14); see (15-20) for discussion. Spectral data from Mars Express contain five unidentified spectral features between 3000 and 3030 cm⁻¹, of which one coincides with the expected position of the CH₄ Q-branch (11,14,21). The data span all seasons and extend over several years, but low S/N ratios require averaging the spectra over two of the three key dimensions (longitude, latitude, time). Other searches featured low spatial (12) or sparse seasonal coverage (12,13), and the results (methane mixing ratios) are best interpreted as upper limits.

We report measurements of methane in Northern Summer 2003 and estimate its source strength and its (short) destruction lifetime. Our search covered about 90% of the planet's surface and spanned 3 Mars years (7 Earth years). Our results (10) are based on simultaneous detection of multiple spectrally-resolved lines of methane, and each observation is spatially resolved, allowing examination of spatial and temporal effects. Our spatial maps reveal local sources and seasonal variations.

To search for methane and other gases on Mars, we used the high-dispersion infrared spectrometers at three ground-based telescopes. Here we report data from CSHELL/IRTF (Hawaii) and NIRSPEC/Keck-2 (Hawaii) (SOM-1). Each spectrometer features a long entrance slit that is held to the central meridian of Mars (Fig. 1A) while spectra are taken sequentially in time (e.g., fig. S1). Pixelated spectra were acquired simultaneously at contiguous positions along the entire slit length, for each observation, providing 35 spectra at 0.2 arc-second (arc-sec) intervals (~ 195 km at disk center) when Mars' diameter is 7 arc-sec (e.g., Fig. 1A). We binned these data (e.g., in groups of 3 along the slit) to provide latitudinally resolved spectra, and then in time (longitude) to improve the S/N ratio (SOM-1). Here, we focus on three dates in 2003 (UT Jan. 12, UT March 19 & 20) and on UT Feb. 26, 2006 (Table 1).

Our spectra exhibit strong lines of terrestrial H_2O ($2\nu_2$ band) and CH_4 (ν_3) along with weaker lines of O_3 ($3\nu_3$) seen against the continuum (Fig. 1B & 1C, top). We corrected the data for telluric extinction (SOM-2). At $3.3 \mu\text{m}$, Mars is seen mainly in reflected sunlight, so the collected spectra also contain Fraunhofer lines (SOM-3). Removing these two components from a composite spectrum exposed the residual Mars atmospheric spectrum (Fig. 1B and 1C) (cf. 22). One line of CH_4 and three distinct lines of H_2O are seen in each panel.

Methane consists of three separate nuclear spin species (A, E, F) that act as independent spectral entities. The identification of two spectrally resolved methane lines (R0 and R1, of the A and F species, respectively) and the good agreement (within measurement error) of the CH_4 column densities obtained independently from each line support our detection (systematic uncertainty and stochastic errors are discussed in SOM-2

and SOM-3). At a later season ($L_s = 220^\circ$), we detected the P2 doublet consisting of lines of the E and F species (SOM-1, fig. S2). Detections (or upper limits) reported by others are based on the intensity summed over the frequencies of multiple unresolved lines [the Q-branch (11), (14)] or on the summed intensity of several undetected individual lines (12, 13).

Column densities and mixing ratios for methane obtained from the spectra of Fig. 1 show a broad methane plume in late-summer when averaged over 46° longitude (Fig. 2A 2B) (SOM-3); using more restricted longitudinal binning shows higher maxima (Fig. 2C, profile 'd'). In early spring (profile 'a'), the CH_4 mixing ratio was small at all latitudes, and showed only a hint of the marked maximum seen in late summer. By early summer (profiles 'b' and 'c'), methane was prominent but the maximum mixing ratio occurred at more northerly latitudes and was somewhat smaller than in late summer. The late summer profile ('d') in Fig. 2C differs from the profile shown in Fig. 2B, owing to different longitudinal binning (23). The mixing ratios shown in Fig. 2C (profile 'd') represent a subset of the data of Fig. 1B, centered at CML 310° (see aspect, Fig. 1A) and binned over only 30 minutes. Including the slit width, 30-minute binning provides a footprint at the sub-Earth point that spans $\sim 16^\circ$ (948 km) in longitude and 10° (586 km) in latitude (fig. S1, Table 1).

A quantitative release rate can be inferred by considering the observed temporal changes (with season) and measured spatial profiles. The summer mixing ratios (profiles b, c, d) show a clear maximum for each north-south spatial profile (Fig. 2C). Moving southward by about 30° from the latitude of the peak, the mixing ratio decreased by a factor of two in each case, and for profile 'd' the northward gradient was similar to the

southward one. These latitudinal gradients suggest that there was a local source(s) and the resulting plume(s) was being dispersed by atmospheric circulation.

We consider the dimension of the hypothesized methane plume to be about 60° in latitude (full width at half maximum, Fig. 2C, profile 'd'), and assume a similar dimension in longitude. The latter view is weakly supported by profiles 'b' and 'c', which differ by 27° in central longitude and by a factor of two in peak mixing ratio. It is also supported by the profile formed by binning over 46° in longitude (277° - 323° , Fig. 2B) which has a peak mixing ratio (24 ppb) reduced by a factor of two from the peak value (45 ppb) obtained when binning over only 16° of longitude (302° - 318° , Fig. 2C, profile 'd'). The slight increase of profile 'd' near 40° N is consistent with enhanced methane (perhaps owing to continued release at that latitude - compare profiles 'b' and 'c'), while the slight increase in profile 'c' near 15° S suggests a small contribution from a source to the west (compare peak position, profile 'd'). Together, these profiles suggest that there may be two local source regions, the first centered near (30° N, 260° W) and the second near (0° , 310° W). The vapor plume from each is consistent with $\sim 60^\circ$ in both latitude and longitude.

The amount of trace gas present in each plume can be estimated from these parameters (SOM-4). In the central plume of profile 'd' (FWHM diameter $\sim 60^\circ$), the mean CH_4 mixing ratio is ~ 33 ppb (120 mol km^{-2}), and the plume contains $\sim 1.17 \times 10^9$ moles of CH_4 ($\sim 1.86 \times 10^7$ kg, or $\sim 19,000$ metric tons). If seasonally controlled, the duration of release must be substantially shorter than 0.5 Mars years, requiring a mean CH_4 release rate $\geq 39 \text{ mol s}^{-1}$ ($\geq 0.63 \text{ kg s}^{-1}$). For comparison, the massive hydrocarbon seep field at Coal Oil Point (Santa Barbara, CA) releases methane at a rate of $\sim 0.4 - 1.0 \text{ kg s}^{-1}$ (24).

We considered three models for plume formation, to constrain aspects of methane

release and its migration in latitude and longitude (SOM-5). A model based on release from a central source region coupled with eddy diffusion fits the observed plume parameters. Models of meridional flow using a GCM (Global Circulation Model) suggest that released gas would move northward by $\sim 3.3 \text{ cm s}^{-1}$ at this season (25), for a total displacement by not more than $\sim 170 \text{ km}$ from its central source. If the mixing coefficients (K_x , K_y) in zonal and meridional directions are identical (K_h), a steady source would fill the plume (profile 'd') in 60 days if $K_h \sim 6.4 \times 10^8 \text{ cm}^2 \text{ s}^{-1}$. For this case, the required source strength was $\sim 3.66 \text{ kg s}^{-1}$. The filling time and K_h vary inversely, whereas K_h and source strength vary proportionately. For a filling time of 0.5 Mars yr (~ 344 Earth days), $K_h \sim 1.1 \times 10^8 \text{ cm}^2 \text{ s}^{-1}$ and the source strength was $\sim 0.63 \text{ kg s}^{-1}$. A reasonable limit for filling time (< 120 days) requires $K_h \sim 3.2 \times 10^8 \text{ cm}^2 \text{ s}^{-1}$ and source strength $\sim 1.8 \text{ kg s}^{-1}$.

These parameters are consistent with release from a single central source region, followed by efficient eddy mixing (SOM-5). The central source could be activated thermally by warming of a surface zone, or by connecting sub-permafrost regions to the atmosphere through seasonally opened pores in scarps or crater walls. The plume would reflect the gross morphology of active release zones (and their intensity), and the peak could suggest a region of enhanced release. For comparison, the sub-Solar latitude was 24° N at $L_s = 122^\circ$ (compare profiles 'b' and 'c') and 10° N for $L_s = 155^\circ$ (profile 'd').

Additional information is obtained from a high-resolution map constructed from our data for mid-summer 2003 (Fig. 3, fig. S1). Methane appears notably enriched over several localized areas: A (East of Arabia Terra, where we also measure greatly enriched water vapor), B1 (Nili Fossae), and B2 (SE quadrant of Syrtis Major). Unusual enrichments of hydrated minerals (phyllosilicates) were identified in Nili Fossae from

Mars Express [(26), (27)] and from the Mars Reconnaissance Orbiter (28) (Fig. 3). The observed morphology and mineralogy [(29), (30)] of this region suggest that these bedrock outcrops, rich in hydrated minerals, might be connecting with reservoirs of buried material rich in volatile species. The characteristic arcuate ridges in the southeast quadrant of Syrtis Major were interpreted as consistent with catastrophic collapse of that quadrant, from interaction with a volatile-rich substrate (30).

The low mean abundance measured in early spring 2006 (profile 'a') provides an important constraint on the methane lifetime. The plume seen in March 2003 (19,000 tons, Fig. 2C profile 'd') implies a global mean mixing ratio of ~ 2 ppb, if later spread uniformly over the planet. The content of the central plume of profile 'c' is similar. Combining data for the entire region mapped during northern summer brings the total methane to 42,000 tons, or 6 ppb if spread uniformly over the planet. However, the mean mixing ratio displayed in early spring equinox in 2006 (profile 'a', Fig. 2C) was only 3 ppb (SOM-3). If methane is not removed by other means, the implied destruction lifetime is ~ 4 Earth years if the 2003 event was singular, to as little as ~ 0.6 Earth years if the event repeats each Mars year. In either case, the destruction lifetime for methane is much shorter than the timescale (~ 350 years) estimated for photochemical destruction [e.g., (12)]. Another process thus must dominate removal of atmospheric methane on Mars and it must be more efficient than photochemistry by a factor ≥ 100 .

Heterogeneous (gas-grain) chemistry is a strong candidate. The presence of strong oxidants in the soil was suggested first by the labeled-release experiment on Viking landers, and laboratory simulations suggested that peroxides (e.g., H_2O_2) were responsible; the apparent discovery of perchlorate (XClO_4) by the Phoenix lander (31,32) suggests the

existence of another family of strong oxidants, although their presence at low latitudes has not been established. Lofting oxidant-coated soil particles into the atmosphere could permit rapid oxidation of CH_4 that collides with them. H_2O_2 is also produced photochemically and is a known trace gas in the atmosphere (33), and (being polar) might bind to aerosol surfaces. Electrochemical processes in dust storms may produce additional peroxide efficiently (4,6,19,20) (SOM-6). Peroxide coated grains might provide an efficient sink for methane for many years thereafter if they settle to the surface and are sequestered in the regolith (6,20). Sequestered oxidants should also efficiently destroy upward-diffusing methane, reducing the fraction that might escape to the atmosphere.

The most compelling question relates to the origin of methane on Mars. The methane we detected is of unknown age – its origin could be ancient (34) or perhaps recent. Both geochemical and biological origins have been explored, but no consensus has emerged. Most theses draw upon known terrestrial analogues such as production in magma [(15, 16)] or serpentinization of basalt [e.g., (35)], or production by psychrophilic methanogenic biota in Mars-analogue cryo-regimes such as permafrost (17). The annual release of methane from an arctic tundra landscape (at 72°N) was measured to be 3.15 g m^{-2} , with mid-summer CH_4 fluxes of typically $30\text{ mg m}^{-2}\text{ day}^{-1}$ (36). If similar release rates applied to our mid-summer plume, the tundra-equivalent-area of (assumed uniform) release would be $\sim 6000\text{ km}^2$ compared with a plume footprint $\sim 9.7 \times 10^6\text{ km}^2$. If methane release were uniform over the plume footprint, the mean release rate could be smaller than the arctic rate by a factor of ~ 1600 .

Of special interest are the deep bio-communities that utilize H_2 (produced by radiolysis of water) as an energy source (reducing CO_2 to CH_4). These communities thrive at 2-3 km

depth in the Witwatersrand Basin of South Africa and have been isolated from the surface (and photosynthesis) for millions of years [(37), (38)]. It might be possible for analogous biota to survive for eons below the cryosphere boundary on Mars, where water is again liquid, radiolysis can supply energy, and CO₂ can provide carbon. Gases accumulated in such zones might be released to the atmosphere if pores or fissures open seasonally, connecting these deep zones to the atmosphere at scarps, crater walls, or canyons. The location of methane maxima over the Syrtis Major shield volcano and the nearby Nili Fossae district suggests a possible relation to serpentinization and/or to the phyllosilicates discovered there [(39), (40)].

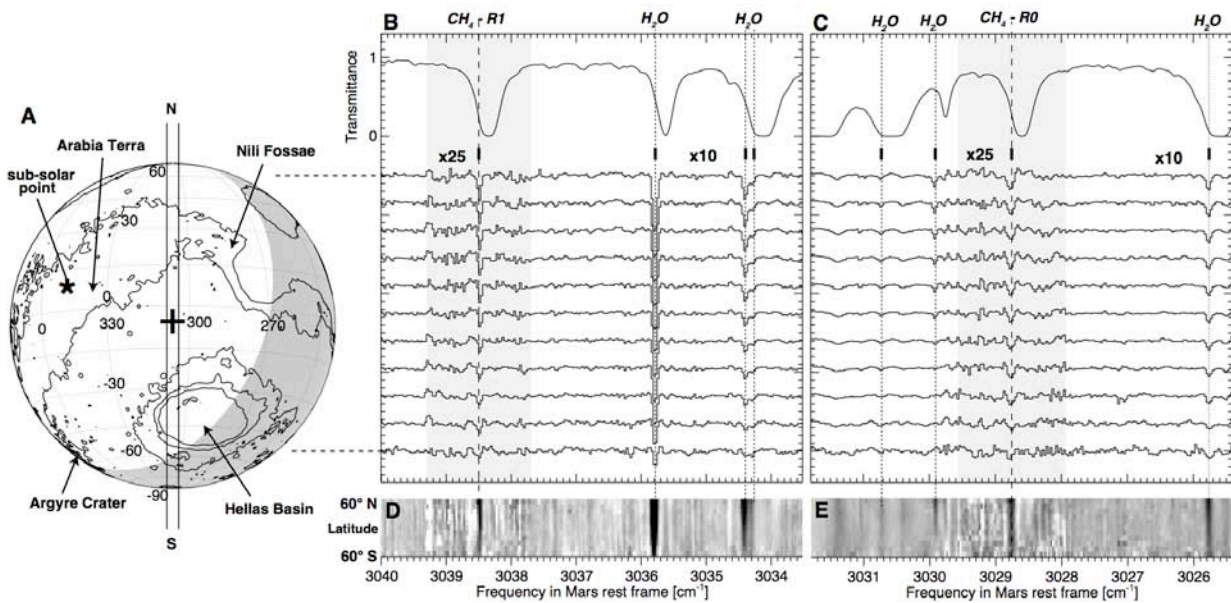


Fig. 1. Detections of methane and water vapor on Mars on UT 19 and 20 March 2003. (A.) Mars is shown as it appeared at the mean time of the R0 and R1 observations (Table 1). The sub-Solar (*) and sub-Earth (+) points are marked, along with several prominent features. Contours of constant altitude are shown at intervals of 3 km, and regions beyond the afternoon terminator (night-side) appear in grey. The entrance slit of the spectrometer was oriented N-S on Mars along the central meridian, and is shown to scale. (B.) Spectra taken on 20 March were extracted at eleven equal intervals (0.6" each) along the slit (ranging from 70° N to 70° S), after binning over longitudes 277° - 323° West. At the sub-Earth position, the binned spectrum samples a footprint 3215 km (E-W) by 586 km (N-S) (see text and SOM-1). Strong lines of terrestrial water and methane (labeled) and weak lines of ozone (e.g., 3036 - 3038 cm⁻¹) appear in a typical spectrum, shown at top of this panel. See (SOM-3) for data reduction. Narrow spectral lines of H₂O (3 lines, small dashes) and CH₄ (the R1 line, long dashes) are seen at the Doppler-shifted positions expected for this date. Corresponding Mars ozone (O₃) absorptions for this date are weak and would appear in the southern polar region (not sampled). (C.) Spectra taken on 19 March are shown as in (B.), but binned over the longitude range 289° - 335°. Spectral lines of H₂O (3 lines, small dashes) and CH₄ (the R0 line, long dashes) are seen. The longitude range sampled was systematically Westward (by 12°) of that sampled for R1 (Table 1), owing to the slower rotation of Mars relative to Earth. The residual spectra shown in Panels B and C are scaled by a factor of either 10 or 25 (grey background), to make the lines more apparent. D and E show residual intensities in a grey-scale format, to visualize more easily the spatial distribution of the gases with latitude. The lines are displayed as measured, i.e., corrections for two-way air mass on Mars (Sun to Mars-surface and Mars-surface to Earth), for Mars local topography, and for terrestrial transmittance have not yet been applied to the residuals (see Fig. 2).

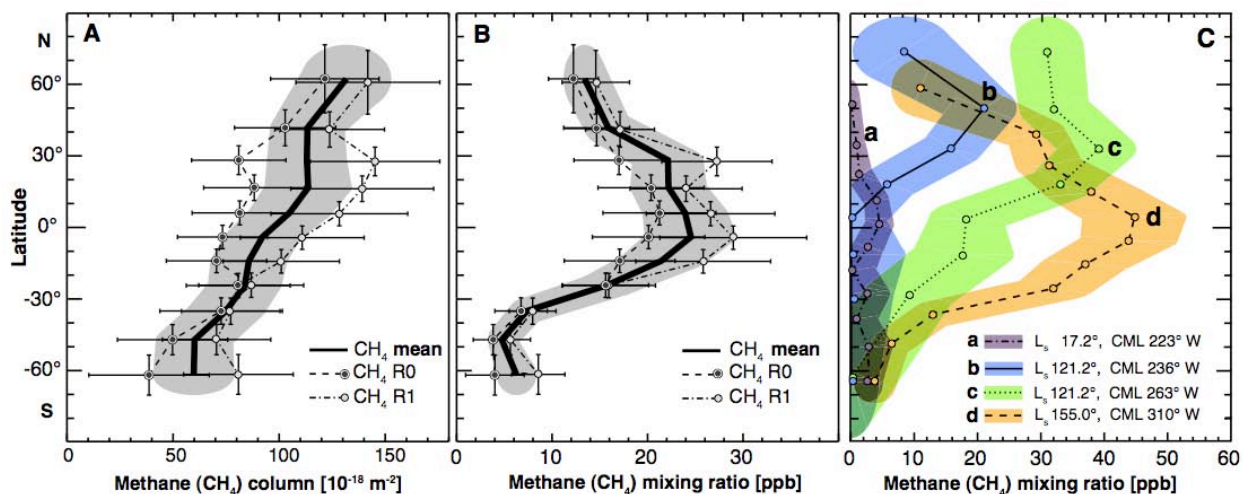


Fig. 2. Absolute abundances, spatial profiles, and seasonal changes of methane on Mars. **(A.)** We show the total CH₄ column density (molecules m⁻²) along a two-way path (Sun to Mars-surface and Mars-surface to Earth) needed to reproduce the measured lines (after correcting for terrestrial transmittance, SOM-2). The R0 (Fig. 1C) and R1 (Fig. 1B) lines were analyzed independently for a range of longitudes that spanned 46° but differed by 12° in mean longitude (312° for R0 vs. 300° for R1, Table 1). The apparent differences in methane column density seen at low-latitudes (30N to 15S) reflect (in part) differences in mean topography sampled on the two dates. The confidence limits contain both systematic uncertainty and random error; the systematic uncertainty affects all extracted values in the same way while the random error introduces scatter among the individual points (SOM-2, SOM-3). **(B.)** We show the local mixing ratio (ppb) of CH₄ obtained from the column density (A) in each footprint, after correcting for two-way air mass on Mars and for topography (SOM-3). The mixing ratios derived from R0 and R1 of CH₄ agree, within confidence limits. The remaining systematic difference at low-latitudes is consistent with stronger weighting of local sources (Fig. 3) on 20 March (R1) when the longitude range sampled was more nearly centered over them. The differences in mixing ratio (R0 vs. R1) should then have decreased with increasing distance from the source(s), as they did (compare values at 60N, 40N, and 25S, 35S, 47S, and 62S). **(C.)** Geographic and temporal variability of Mars methane. We show latitudinal profiles of methane mixing ratios for different longitudes and seasons; the width of the color envelope represents the ± 1-σ confidence envelope. The areocentric seasons (L_s) are: early Northern Spring (**a**: 17°), early Northern Summer (**b**, **c**: 122°), late Northern Summer (**d**: 155°) (Table 1). These extracts are taken from spectra centered at the indicated longitude (CML), and the sub-Earth footprints span longitude-latitude ranges (Table 1) with these physical dimensions: **a**: 770 km x 535 km, **b**, **c**: 1274 km x 818 km, **d**: 948 km x 586 km. The mixing ratios shown in profile 'd' are larger than those shown in Fig. 2B owing to different longitudinal binning, and they reflect the longitudinal maximum of the plume [SOM-1, fig. S1, S6, Fig. 3].

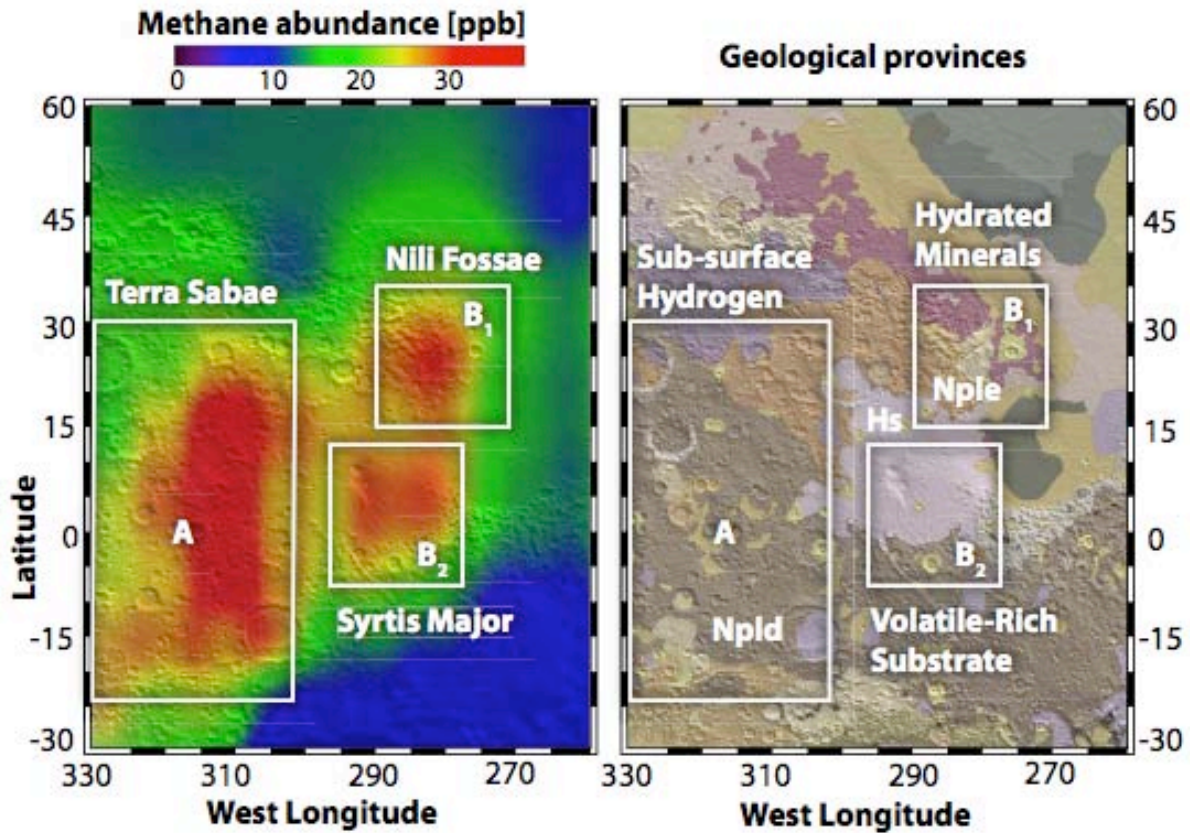


Fig. 3. Regions where methane appears notably localized in Northern Summer (A, B1, B2), and their relationship to mineralogical and geo-morphological domains. (A.) Observations of methane near the Syrtis Major volcanic district. (B.) Geologic map of Greeley and Guest (41) superimposed on the topographic shaded-relief from MOLA (42). The most ancient terrain (Npld, Nple) is Noachian in age (~3.6 - 4.5 billion years old, when Mars was wet), and is overlain by volcanic deposits from Syrtis Major of Hesperian (Hs) age (~3.1 - 3.6 billion yrs old). See text.

Table 1. Observational searches for Mars methane on selected dates^a.

Date & observation range [UT]	Mars Season [L_s , °]	Longitude Range [CML, °]	Doppler Shift [km s^{-1}]	CH ₄ Line Searched	Footprint ^b (°long by °lat)
2003 – Mars Year (MY) 26					
11 Jan 19:36-20:34	121.5	274 - 288	-14.7	R1	22° x 14°
12 Jan 17:20-20:18	121.9	231 – 274	-15.0	R1	22° x 14°
13 Jan 17:05-20:07	122.4	218 - 262	-15.0	R0	22° x 14°
19 Mar 15:41-18:50	154.5	289 – 335	-15.7	R0	16° x 10°
20 Mar 15:34-18:44	155.0	277 - 323	-15.6	R1	16° x 10°
2006 – Mars Year (MY) 27-28					
16 Jan 04:49-07:03 ^c	357.3	303–336	+16.1	R0, R1	
26 Feb 01:28-02:53	17.2	223–244	+17.1	R1	13° x 10°

a. A complete listing of all dates searched, spanning 7 years, is available from the authors.

b. Centered on the sub-Earth point, binned over 30-minutes in time and 0.6'' along the slit.

c. Using NIRSPEC/Keck (SOM-3), all other listed observations used CSHELL/IRTF.

Endnotes for Main Text:

- ¹ H. Nair, M. Allen, A. D. Anbar, Y. L. Yung, R. T. Clancy, *Icarus* **111**, 124 (1994).
- ² M. E. Summers, B. J. Lieb, E. Chapman, Y. L. Yung, *Geophys. Res. Lett.* **29**(24), 2171 (2002).
- ³ Ah-S. Wong, S. K. Atreya, T. Encrenaz, *J. Geophys. Res. (Planets)* **108** (E4), 7-1 (2003).
- ⁴ S. K. Atreya *et al.*, *Astrobiology* **6** (3), 439 (2006).
- ⁵ R. E. Pellenbarg, M. D. Max, S. M. Clifford, *J. Geophys. Res. (Planets)* **108** (E4), GDS 23-1 (2003).
- ⁶ S. K. Atreya, P. R. Mahaffy, and Ah-S. Wong, *Planet. Sp. Sci.* **55**, 358 (2007).
- ⁷ W. C. Maguire, *Icarus* **32**, 85 (1977).
- ⁸ V. A. Krasnopolsky, G. L. Bjoraker, M. J. Mumma, D. E. Jennings, *J. Geophys. Res.* **102** (E3), 6525 (1997).
- ⁹ M. Lellouch *et al.*, *Planet. Sp. Sci.* **48** (12-14), 1393 (2000).
- ¹⁰ M. J. Mumma *et al.*, *Bull. Am. Astron. Soc.* **35**, 937 (2003); **36**, 1127 (2004); **37**, 669 (2005); **39**, 471 (2007); **40**, 396 (2008).
- ¹¹ V. Formisano, S. Atreya, T. Encrenaz, N. Ignatiev, M. Giuranna, *Science* **306**, 1758 (2004).
- ¹² V. A. Krasnopolsky, J. P. Maillard, T. C. Owen, *Icarus* **172**, 537 (2004).
- ¹³ V. A. Krasnopolsky, *Icarus* **190**, 93-102 (2007).
- ¹⁴ A. Geminale, V. Formisano, M. Giuranna, *Planet. Sp. Sci.* **56**, 1194 (2008).
- ¹⁵ J. R. Lyons, C. E. Manning, C. E. Nimmo, *Geophys. Res. Lett.* **32**, L13201(2005).
- ¹⁶ C. Oze and M. Sharma, *Geophys. Res. Lett.* **32**, L10203 (2005).
- ¹⁷ T. C. Onstott *et al.*, *Astrobiology* **6** (2), 377 (2006).
- ¹⁸ V. A. Krasnopolsky, *Icarus* **180**, 359 (2006).
- ¹⁹ W. M. Farrell, G. T. Delory, S. K. Atreya, *Geophys. Res. Lett.* **33**, L21203 (2006).
- ²⁰ G. T. Delory *et al.*, *Astrobiology* **6** (3), 451 (2006).
- ²¹ V. Formisano *et al.*, *Planet. Sp. Sci.* **53**, 1043-1052 (2005).
- ²² G. L. Villanueva, M. J. Mumma, R. E. Novak, T. Hewagama, *Icarus* **195**, 34 (2008).
- ²³ We binned spectra over 46° degrees of longitude (centered at CML 300°) for Fig. 1B & C (and 2A & B), but over only 16° for Fig. 2C. Profile 'd' is centered at CML 310°, leading to lower mean mixing ratios in Fig. 2B compared with Fig. 2C (profile 'd'). See detailed map in Fig. 3.
- ²⁴ S. Mau *et al.*, *Geophys. Res. Lett.* **34**, L22603 (2007).
- ²⁵ M. A. Mischna, M. I. Richardson, R. J. Wilson, D. J. McCleese, *J. Geophys. Res.* **108** (E6), 5062, 16-1 (2003).
- ²⁶ F. Poulet *et al.*, *Nature* **438**, 623 (2005).
- ²⁷ J. P. Bibring *et al.*, *Science* **312**, 400 (2006).
- ²⁸ J. F. Mustard *et al.*, *Nature* **454**, 305 (2008).
- ²⁹ H. Hiesinger and J. W. Head III, *J. Geophys. Res.* **109**, E01004 (2004).
- ³⁰ D. Baratoux *et al.*, *J. Geophys. Res.* **112**, E08S05 (2007).
- ³¹ M. H. Hecht *et al.*, *Eos* **89**(52), Fall Meeting Suppl., Abstr. U14A-04 (2008).
- ³² S. P. Kounaves *et al.*, *Eos* **89**(52), Fall Meeting Suppl., Abstr. U14A-05 (2008).
- ³³ T. Encrenaz *et al.*, *Icarus* **195**, 547 (2008).
- ³⁴ M. D. Max, S. M. Clifford, *J. Geophys. Res.* **105**, 4165 (2000).
- ³⁵ D. S. Kelley *et al.*, *Science* **307**, 1428 (2005).
- ³⁶ C. Wille, L. Kutzbach, T. Sachs, D. Wagner, and E.-M. Pfeiffer, *Global Change Biol.* **14**, 1395 (2008).
- ³⁷ T. C. Onstott *et al.*, *Geomicrobiol. J.* **23**(6), 369 (2006).
- ³⁸ B. Sherwood Lollar *et al.*, *Chem. Geol.* **226**, 328 (2006).
- ³⁹ J.-P. Bibring *et al.*, *Science* **312**, 400 (2006).
- ⁴⁰ J. F. Mustard *et al.*, *Nature* **454** (7202), 305 (2008).
- ⁴¹ R. Greeley and J. E. Guest, *U.S. Geol. Surv. Map I-1802-B* (1987).
- ⁴² D. E. Smith *et al.*, *J. Geophys. Res.* **106**(E10), 23689, (2001).
- ⁴³ We thank T. C. Onstott for helpful comments, and two anonymous referees for their comments and suggestions. This work was supported by NASA [Planetary Astronomy Program (RTOP 344-32-07 to M.J.M), Astrobiology Institute (RTOP 344-53-51, to M.J.M), and Postdoctoral Program (G.L.V.)] and by NSF [Research at Undergraduate Institutions Program AST-0505765, to R.E.N.]. We thank the Director and staff of NASA's InfraRed Telescope Facility (operated for NASA by the University of Hawaii) for exceptional support throughout our long Mars observing program. Data were also obtained at the W. M. Keck Observatory, operated as a scientific partnership by CalTech, UCLA, and NASA.

Supporting On-line Material for

**Strong Release of Methane on Mars in Northern
Summer 2003**

Michael J. Mumma,^{1*} Geronimo L. Villanueva,^{2,3} Robert E. Novak,⁴
Tilak Hewagama,^{3,5} Boncho P. Bonev,^{2,3} Michael A. DiSanti,³
Avi M. Mandell,³ and Michael D. Smith³

¹ NASA Goddard Space Flight Center, Mailstop 690.3, Greenbelt, MD 20771, USA

² Department of Physics, Catholic University of America, Washington DC, 20008

³ NASA Goddard Space Flight Center, Mailstop 693, Greenbelt, MD 20771, USA

⁴ Department of Physics, Iona College, New Rochelle, NY 10801, USA

⁵ Department of Astronomy, University of Maryland, College Park, MD 20742-2421, USA

* To whom correspondence should be addressed. E-mail michael.j.mumma@nasa.gov

Published

DOI:

This PDF file includes:

SOM Text

Fig. S1 to S6

References and Notes

Supporting Text

SOM-1:

Our current dataset of biomarker gases extends over a period of 10 years, and was acquired primarily with two instruments: CSHELL (Cryogenic Echelle Spectrograph [1, 2]) at NASA-IRTF (Infrared Telescope Facility) and NIRSPEC (Near Infrared Spectrograph [3]) at Keck-2. The third instrument used (Phoenix spectrometer at Gemini South) suffered from internal scattered light, especially for a very bright source such as Mars; we were not able to remove that artifact fully, and so defer discussion of Phoenix data to a future publication.

Observing from a high altitude site (e.g., Mauna Kea, HI) reduces extinction by terrestrial methane, and (especially) by condensable species (H_2O and HDO). A significant wavelength shift further reduces extinction by terrestrial counterparts, and so we target Mars when its line-of-sight velocity is large (e.g., >10 km/sec when searching for CH_4).

Most of the observations were performed using CSHELL/IRTF, which features an instrumental resolving power of 40,000, a sampling rate of 100,000, and a spectral bandwidth of 7 cm^{-1} at 3000 cm^{-1} . Since the width of the Martian lines ($\sim 0.004 \text{ cm}^{-1}$) is much narrower than the instrumental resolution ($\sim 0.08 \text{ cm}^{-1}$), the observed line shapes are defined by the instrument's transfer function with a spectral width of 2 to 4 pixels (see Fig. 1 of main manuscript). The instrument is very stable in frequency, with maximum observed spectral displacements of 0.004 cm^{-1} (or 0.13 pixels) in 30 minutes. All data presented in this paper have been organized and processed in sets of 30 minutes or less, and therefore these micro-deviations do not affect the residual spectra.

We followed our standard observing methodology, orienting the spectrometer entrance slit North-South on the planet and using the narrowest available slit (0.5×30 arc-sec with CSHELL and 0.144×12 arc-sec with NIRSPEC) to maximize the spectral resolving power. The spatial scale is 0.2 arc-sec per pixel for CSHELL and 0.198 arc-sec for NIRSPEC, and both slits are longer than the planetary diameter (7 arc-sec in March 2003). We nodded each telescope along the slit in a sequence of four scans (ABBA) with an integration time of 1 minute per scan. CSHELL observations sampled Mars in both positions along the slit (A and B separated by 15 arc-sec), allowing maximum efficiency. With the shorter NIRSPEC slit, we sampled Mars only in the A position and nodded 30 arc-sec along the slit to a sky position (B). The sum (A – B – B + A) removed telluric and other parasitic emissions, presenting the Mars spectral-spatial information for further analysis. At each grating setting, flat-field and dark frames were obtained immediately afterward for data calibration purposes. The sensitivity of the resulting spectra is mainly defined by photon noise statistics. A typical 60-second Mars exposure will lead to a signal (S) of 1000 counts [ADU/pixel] on the detector, and a corresponding noise (N) equal to $\sqrt{S/G} = 9.5$ [ADU/pixel], where $G = 11$ electrons/ADU (CSHELL's detector gain). A typical set of 20 minutes on source and integrated over 3 pixels along the slit, would correspond to a S/N ratio of 815 or a precision of 0.12%.

The spatial resolution of our measurements is restricted by the point-spread-function (PSF) of the observations (which is determined by the combined effects of diffraction and atmospheric seeing) and by guiding inaccuracies. To correct guiding error, exposures were processed individually and then were registered to an established fiducial position before co-addition of frames. Positioning errors due to differential refraction are minimized since these spectrometers

are designed to guide using a broadband image sampled at a comparable wavelength. To reproduce the continuum spatial profile observed along the N-S meridian, we assumed a “Lambertian” surface and included two components in the emergent intensity: reflected sunlight and thermal emission from the surface. This permitted improved alignment of the frames, and provided higher precision when pixelated spectra were mapped into latitude-longitude positions on the planet.

SOM-2:

In our early investigations (before 2005), we removed telluric absorption features by extracting the Mars spectrum at one position along the slit, and subtracting it from spectra measured at other positions. This approach worked well for water vapor. However, it significantly reduced the intensity of the residual spectral lines for well-mixed species on Mars (e.g., CO₂), and demonstrated the need to extract absolute abundances for trace species such as methane. The extraction of absolute spectral signatures is, however, extremely complex. It requires precise frequency calibration (better than ten milli-pixels), along with synthesis of the telluric transmittance at very high spectral resolution [approaching 100 m/sec (or 0.001 cm⁻¹ at 3000 cm⁻¹)].

Since 2005, we re-designed our spectral analysis software to achieve absolute extractions (4,5). We developed new techniques to account for instrumental effects, thereby permitting an order of magnitude increase in sensitivity in processed spectra. Our current tools include correction (with milli-pixel precision) of spatial and spectral distortions introduced by anamorphic optics in the spectrometers, removal of internal scattered-light, correction of variable resolving power (along the slit and along the dispersion direction), removal of spectral fringing (using Lomb periodogram analysis), correction of residual dark current, and correction of residual telluric radiance.

We incorporated new models for synthesizing (at sub-Doppler resolution) atmospheric transmittance on Earth and Mars that together form the basis for absolute extractions. We now compare the observed sky radiance with spectra synthesized using a rigorous line-by-line, layer-by-layer radiative transfer model of the terrestrial atmosphere (GENLN2, version 4 [6]). Several improvements were introduced to this terrestrial atmospheric model [4,7,8], and it now properly accounts for spectral pressure shifts. The molecular database accessed by the model was also updated to include the latest spectroscopic parameters [8]. In particular, recently corrected and extended parameters for H₂O and C₂H₆ species [9] were included.

Systematic uncertainty and Random errors:

Systematic uncertainty can be introduced by errors in the synthetic model for terrestrial transmittance, for example by errors in the molecular line parameters, errors in abundance of contributing chemical species (especially if omitted entirely), and errors in emission/absorption processes. It can also be introduced by electronic effects, such as print-through of clocking signals in the CCD detectors.

To remove the most significant systematic uncertainties, we formed a background spectrum (based on our 7 years of data) and removed it from the reduced spectra. The background spectrum was computed by averaging over all spectral residuals (after removing real martian lines), and it corrected systematic errors arising from uncertainties in the molecular parameters used to calculate the terrestrial transmittance spectra. The background spectrum was comparable

in intensity (standard deviation of 0.13%) to the instrumental photon noise (typically a standard deviation of 0.12%); because the background was removed from all spectra, it did not introduce spatial variations in the final spectra.

Although reduced by this approach, some systematic effects remained. In Figs. 1D & 1E, we show gray-scale images of the spectral residuals row-by-row along the slit (after removing the "background spectrum"). Remaining systematic errors can be recognized in 1D & 1E as columns that are whiter or blacker than the mean (e.g., in the range 3034.5 - 3035.6 cm^{-1}). For each row, we formed the RMS of spectral residuals and adopted this as a measure of the combined random and systematic errors in that row (we except columns containing observed or expected CH_4 and H_2O lines). We then combined the errors for the three spatial rows and three spectral columns representing the detection (shown for a given latitude bin in Fig. 2A), and we expressed the "error" as an equivalent column density. Close inspection reveals that systematic errors form a major component of the total error budget. However, systematic errors tend to be correlated from row to row, and thus do not affect the scatter amongst the points of Fig. 2A greatly.

Random errors arise mainly from stochastic noise of the (total) photon stream accumulated for each spectral extract, and the amount varies with spectral position. At spectral positions removed from strong terrestrial lines, Mars is brighter than the terrestrial foreground so it dominates the stochastic noise there. In the cores of strong terrestrial lines (CH_4 , H_2O), (weaker) terrestrial emission dominates so the noise is smaller there. The actual stochastic noise at the position of Mars CH_4 lines is intermediate to these two values and it depends on the specific Doppler-shift when Mars was observed. The combined photon number is nearly independent of position along the slit, thus the $1\text{-}\sigma$ stochastic noise levels (noise-equivalent column abundance) are nearly the same for points in Fig 2A, though we reiterate that systematic error comprises the greater part of the total error budget.

In contrast with Fig. 2A, the $1\text{-}\sigma$ confidence levels (noise-equivalent mixing ratio) in Fig. 2B differ from one another, because both the two-way airmass on Mars and the topographic correction differ point-by-point along the slit.

SOM-3:

We co-measure multiple spectral lines of water vapor in both methane settings (Fig. 1B and 1C). The extracted spectra were binned over longitude ranges (Table 1) centered at the indicated CML and by 3-pixels along the slit (0.6"), but the latitudinal extent of the spectral bins differs slightly as Mars' apparent diameter changes (4.8" for profiles 'b' & 'c', 6.95" for profile 'd', and 10" for profile 'a') (Table 1). The residuals are also represented as grey-scale maps in Figs. 1D and 1E, which reveal strong latitudinal gradients for both gases. Water vapor is concentrated in the Northern hemisphere, as expected for this season ($L_s = 155^\circ$, or late summer in the North). From the measured line intensities, we derived the water vapor column on Mars by using a Levenberg-Marquardt retrieval algorithm and a multi-layer planetary radiative transfer model (CODAT package) for calculating the synthetic spectra. The local atmospheric conditions (pressure and temperatures) fed to the radiative transfer model were calculated using the LMD-AOPP-IAA general circulation model [10], a non-linear, global and three-dimensional hydrodynamic model of the Martian atmosphere.

The retrieval of molecular abundances includes corrections for double path absorption (Sun-to-surface and surface-to-observer air masses) and surface thermal emission for one-way (surface-to-observer) absorption only. At these wavelengths, the radiation received from Mars is a combination of reflected-sunlight (with Fraunhofer lines) and planetary thermal emission (featureless continuum). Sparse spectral lines of Mars' atmospheric constituents are superposed on the continua according to the optical path sampled by the two components (Fig. 1).

The varied surface temperatures and albedos across the Mars surface lead to differences in the apparent thermal/solar ratio, and thus in the apparent equivalent width of the observed Fraunhofer lines. By comparing residual spectra of Mars to the solar spectrum measured by the ATMOS instrument [11,12], we estimated the ratio of the thermal and solar components pixel-by-pixel along the slit [13]. We retrieve the true vertical column density which gives rise to the observed Mars lines, by correcting for the double path atmospheric extinction of solar radiation (with appropriate incidence and viewing angles) and for one-way extinction of surface thermal emission.

We constructed a multi-layer model for Mars' atmosphere and extracted the column density (molecules cm^{-2} along the two-way path traversed by reflected sunlight, i.e., the sum of Sun-to-Mars-surface and Mars-surface-to-Earth) needed to reproduce the lines (CH_4 R1, R0; H_2O) seen in the measured spectral residuals of Figures 1B and 1C. We then calculated the zenith column density for each spatial footprint, and obtained mixing ratios by comparing our retrieved zenith column densities (CH_4 , H_2O , etc.) with the CO_2 column for that footprint. We validated this approach for relevant dates (Table 1) by comparing parameters retrieved from our spectral data with those measured from Mars orbit by TES (14,15) (e.g., H_2O on UT 16 January 2006; Table 1, Fig. S4). We also compared with predictions of two General Circulation Models (10,16) tailored for the local time on Mars and using MOLA (17,18) altitudes averaged over each footprint (Fig. S3, S5). The agreement for surface pressure and temperature is within errors of the GCM data. Our extracts for H_2O also agree well with those measured by TES over the interval 15-25 March 2003 and averaged over each spatial footprint. These comparisons validate our approach and demonstrate that reliable absolute abundances are recovered. The equivalent widths of our measured methane lines are the same order of magnitude as the retrieved water lines indicating the validity of our approach for determining the absolute methane abundance.

In Fig. S6, we compare spectra for the four data sets represented in Fig. 2C. Spectral extracts for each date were averaged over latitudes 5° - 50° N, further improving the signal-to-noise ratio in the mean spectra and more clearly revealing the molecular lines (CH₄ and H₂O). These extracts reveal that individual line intensities change significantly with location on the planet and with season. The observed behavior of H₂O lines shows that atmospheric water vapor is negligible at the beginning of northern spring, but increases strongly as the surface warms and surface ices vaporize; this behavior has long been known from spacecraft and ground-based measurements (14, 19,20,21). Methane also varies greatly – we find only a suggestion of the R1 line in early spring (a), but a strong detection by early summer (b, c) and a further increase by late summer. The small mean mixing ratio (3 ± 1 ppb, over 15° N - 60° S) seen in profile 'a' (Fig. 2C) places strong constraints on models for methane release and destruction (see main text). The spectral extracts for early summer ('b' & 'c' in Fig. S6) reveal strong changes in the CH₄ R1 line with longitude, reflecting the changing abundance ratios revealed by spatial profiles for methane (profiles 'b' & 'c' in Fig. 2C).

The algorithm used to retrieve the molecular abundances was the gradient-expansion least-squares algorithm (Marquardt). This well established method combines the advantages of the gradient search for the first portion of the search and behaves more like an analytical solution as the search converges (22). It finds the solution efficiently, directly and is practically insensitive to the initial conditions.

The goodness of the fit was calculated in the standard fashion as:

$$\chi_v^2 \equiv \frac{1}{N-m} \sum \left\{ \frac{1}{\sigma_i^2} [y_i - f(x_i)]^2 \right\}$$

where N is the number of pixels in the spectrum, m is the number of parameters (abundances) being fitted, σ_i represents the individual uncertainty of pixel i, y_i is the residual transmittance intensity, $f(x_i)$ is the synthetic model computed using multi-layer planetary radiative transfer model (described above), and x_i is the frequency of pixel 'i'. In a perfect fit ($y=f(x)$), χ_v^2 is equal to 1 if the defined uncertainties (σ_i) are equal to the 'true' uncertainty of the points. Because of the selected binning of our data and quality of the residuals, we are mostly dominated by photon noise statistics, so $\sigma_i \sim$ photon noise. Nevertheless, errors in the computation of residuals will lead to additional sources of uncertainty, and for that reason we compute for each residual spectrum the 'true' standard deviation of the points (σ , which includes photon-noise error and instrumental/modeling uncertainties). Our uncertainties ($\sigma_i = \sigma$), therefore, include all quantifiable sources of intensity error, and consequently the resulting χ_v^2 is by definition equal to 1. The uncertainty of the retrieved parameters (CH₄, H₂O, CO₂ abundances) is then calculated in terms of the curvature of χ_v^2 function in the region of minimum using the standard error propagation analysis of the gradient-expansion least-squares algorithm.

Uncertainties can also be introduced by errors in the assumed atmospheric conditions. The temperature errors of the GCM are less than 5K (if compared to values retrieved by MGS/TES), while the pressure uncertainty is estimated to be lower than 0.03 mbar (23). The uncertainty in surface pressure will lead to errors of ~0.5% in abundance for a typical 6 mbar surface pressure, while a 5K error in the temperature would affect abundances retrieved from the R1 line by less than 4%. These uncertainties are smaller than those defined by the intrinsic sensitivity of measurements.

Our absolute retrievals of water vapor column densities agree well with TES data averaged over the same spatial footprints, for the latitude ranges sampled (Fig. S4). Moreover, our absolute retrievals of surface pressure and gas temperature (at the surface and in the first scale height) agree well with TES data and GCM models (Fig. S5). Together, they validate the rigor of our observational, data reduction, and analytical approaches.

SOM-4:

The mean diameter of Mars is ~ 6790 km, so a 60° arc along a great circle spans ~ 3555 km on the surface. Points that are 30° (1800 km) distant from a central locus enclose a surface area (A_s) of $\sim 9.7 \times 10^6$ km², representing $\sim 6.7\%$ of Mars' entire surface area (1.45×10^8 km²). The mean column density of Mars' atmosphere is $\sim 2.2 \times 10^{23}$ molecules cm⁻² or ~ 0.365 mol cm⁻², so a trace gas with mean mixing ratio of 1 ppb then represents ~ 3.65 mol km⁻². At 1 ppb, A_s then contains 3.54×10^7 moles of the trace gas.

SOM-5:

The presence of a well-defined peak in mixing ratio with latitude (e.g., near 0° N in profile 'd') coupled with (approximately equal) concentration gradients towards the North and South caused us to consider (first) steady release from a central source with radial expansion driven by the observed concentration gradients (Model 1). A simple model demonstrated that the time scale for filling the plume by Fick's diffusion is very long ($\sim 10^7$ years); persistence of the plume over this long interval is required but is not supported by our observations. We next considered release from multiple individual release zones distributed over a large region, with Fickian diffusion filling the gaps between local 'hot-spots' (Model 2). The diffusion radius around a local 'hot-spot' develops at a rate ~ 10 cm yr⁻¹, so a source region with 'hot-spots' separated by a modal spacing of 5 cm would fill rapidly after seasonal turn-on and the profile would appear relatively 'smooth' after 3 months. However, such small-scale structure could never be discerned at our spatial resolution (e.g., profile 'd'). While Model 2 is not eliminated by our data, strong local gradients in the density of 'hot spots' (or a continuous zone of release) are needed to produce the observed plume properties.

We then considered release from a central source region coupled with eddy diffusion (Model 3) that is often invoked to explain rapid mixing over large spatial scales. Efficient (vertical) eddy diffusion is needed to mix methane rapidly in the first few scale heights above the surface, but (much more efficient) horizontal eddy mixing is needed to effect the large meridional and zonal size of the plume. Estimated values for the vertical eddy coefficient range widely: the mean value derived from dust profiles in the lower atmosphere was $1.1 (\pm 0.5) \times 10^6$ cm² s⁻¹ (at sunset, Phobos 2 [24]), while a recommended value of 10^7 cm² s⁻¹ was inferred from O₂ and H₂ abundances (25) and a value larger than 10^7 cm² s⁻¹ provided a best fit to the measured abundance of H₂O₂ (26). A value of 10^7 cm² s⁻¹ would ensure uniform mixing over two scale heights in ~ 5 sols (27,28). Meridional (horizontal) mixing coefficients derived from the observed reduced enhancement of polar Argon are much larger, $\sim 1.4 \times 10^9$ cm² s⁻¹ in March 2003 ($L_s = 155^\circ$) (29,30).

We also considered release from a polar ice that is seasonally stable (winter) but becomes unstable in early spring, releasing CH₄ and H₂O (Model 4). Seasonal streaming of CO₂ and eddy diffusion are required to explain rapid transport of water vapor from the seasonal polar cap to

mid-latitude regions (31). Entrainment of CH₄ in the CO₂-H₂O stream could explain a rapid dissemination of released methane and perhaps produce a mixing ratio profile whose peak moves southward as the season advances into mid- and then late summer. The northward gradient that develops by late summer (profile 'd') could then reflect decreasing release from the seasonal polar cap. However, the longitudinal gradients seen in our data may require corresponding longitudinal enhancements of methane sourced at high latitudes.

SOM-6:

High electric fields develop at edge gradients of individual grains, ultimately permitting electric discharges that (in dust storms) might destroy methane directly (32) and might also produce H₂O₂ through ensuing chemical reactions (33,34). If so produced, H₂O₂ then could condense onto airborne grains where CH₄ could react with it, producing the principal oxidation products methanol (CH₃OH) and formaldehyde (H₂CO) (these species have short photochemical lifetimes on Mars and are rapidly removed).

Supporting Figures:

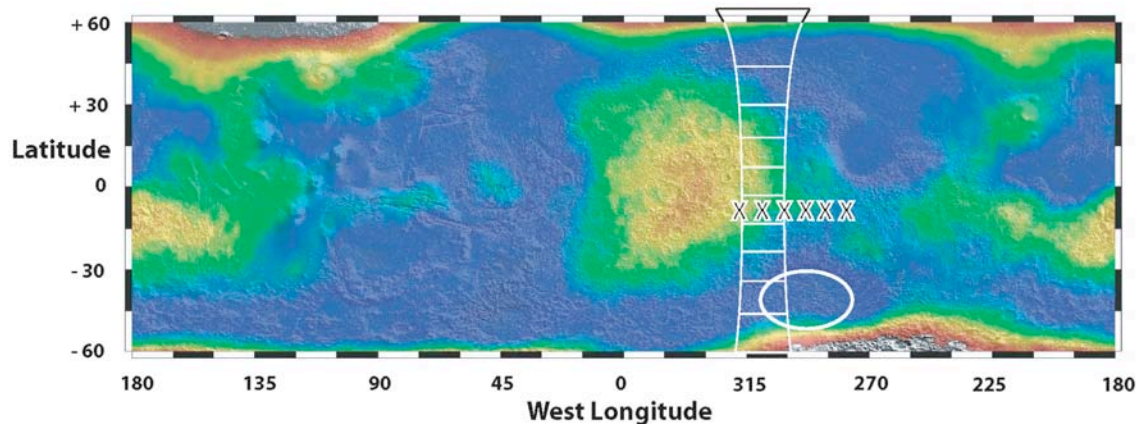


Figure S1: Spatial footprints for spectral extracts are shown projected onto a latitude-longitude map of Mars (West longitude system). We used the narrowest CSHELL slit (0.5" wide) to obtain the highest possible spectral and spatial resolution. On UT 20 March 2003, the slit width projected onto the planet (6.95" diameter) represented 448.5 km (E-W), or 8.24° longitude at the sub-Earth point. The CML advances at a rate of 14.6° degrees per hour, so the slit edges traverse a range of longitudes 15.54° in 30 minutes. Each pixel extends 0.2" along the slit (N-S), so a 3-pixel spectral extract projects onto 586 km (N-S), or 9.87° of latitude at the sub-Earth point. The footprints for 10 spectral bins (CML 310° W, 30 minutes elapsed time) are outlined in white, and the CMLs of successive extracts are marked (X) at 30-minute intervals. The 11 spectra shown in Fig. 1 are binned over 190 minutes elapsed time and thus represent a footprint 3215 km x 586 km at the sub-Earth point. Profile 'd' (Fig. 2C) represents spectra centered at CML 310°, and binned over 30 minutes. The rim of the Hellas impact basin is shown as a white oval, and the sub-surface hydrogen abundance is color-coded, for comparison [35].

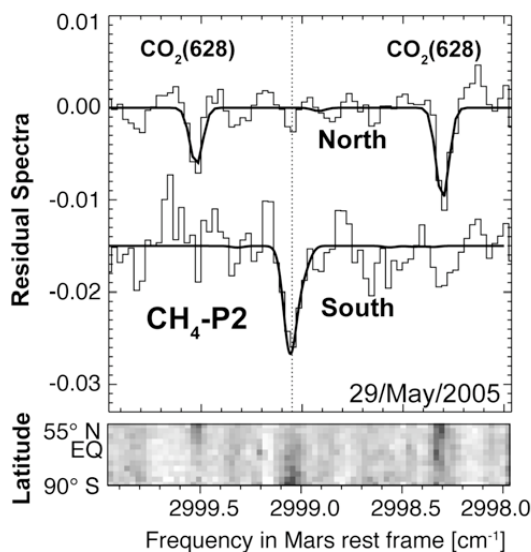


Figure S2: Detection of the CH₄ P2 doublet of the ν_3 band (consisting of lines of the E and F nuclear spin species) in May 2005 ($L_s = 220^\circ$). Two lines of a newly discovered band ($\nu_2 + \nu_3$) of $^{16}\text{O}^{12}\text{C}^{18}\text{O}$ (628) are seen in the northern hemisphere (4). The CO₂ lines are stronger at high atmospheric temperature. The dark solid lines are simulated spectra.

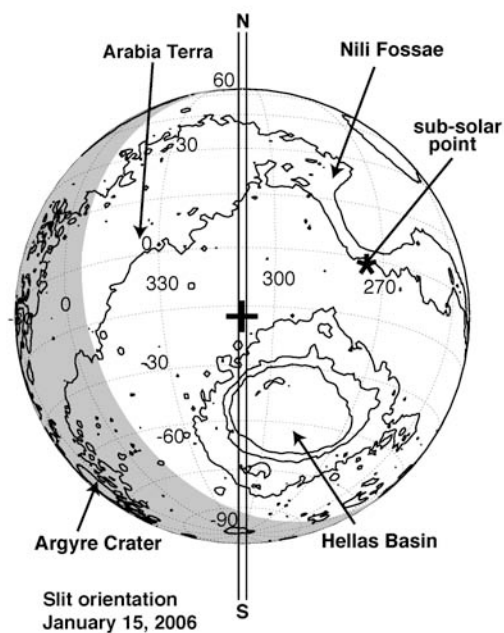


Figure S3. The aspect of Mars as seen from Earth on UT 16 January 2006 ($L_s = 357^\circ$). The apparent diameter was 10 arc-seconds, and the sub-solar point is indicated. The NIRSPEC entrance slit is positioned along the central meridian longitude. Spectra were acquired at intervals of 0.2 arc-seconds along the slit, and binned to 0.6 arc-second intervals. Contours of constant altitude are shown at intervals of 3 km.

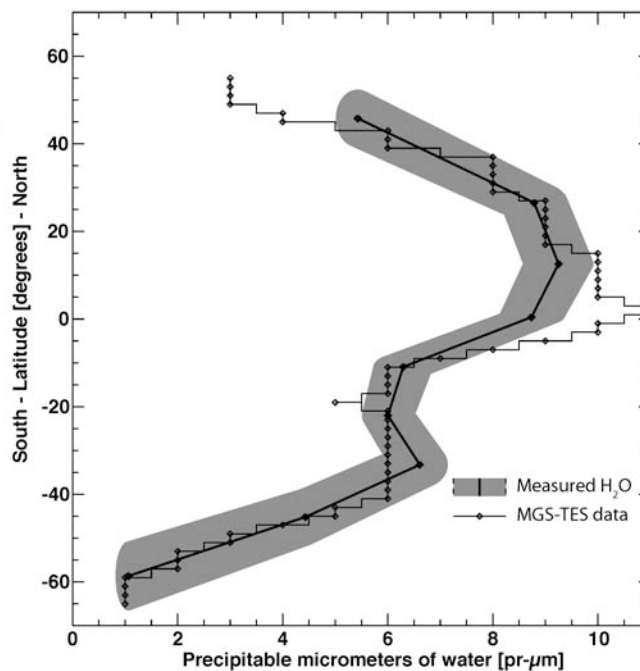


Figure S4. The column density of H_2O retrieved from NIRSPEC binned spectra (full line) is compared with measurements obtained by TES (14) on the MGS orbiter for this season (points, histogram). Diurnal differences between our measurements at 10:00 and the MGS-TES at 14:00 were reconciled by multiplying our values by 1.25. The NIRSPEC and TES results agree well with a high correlation of 96%.

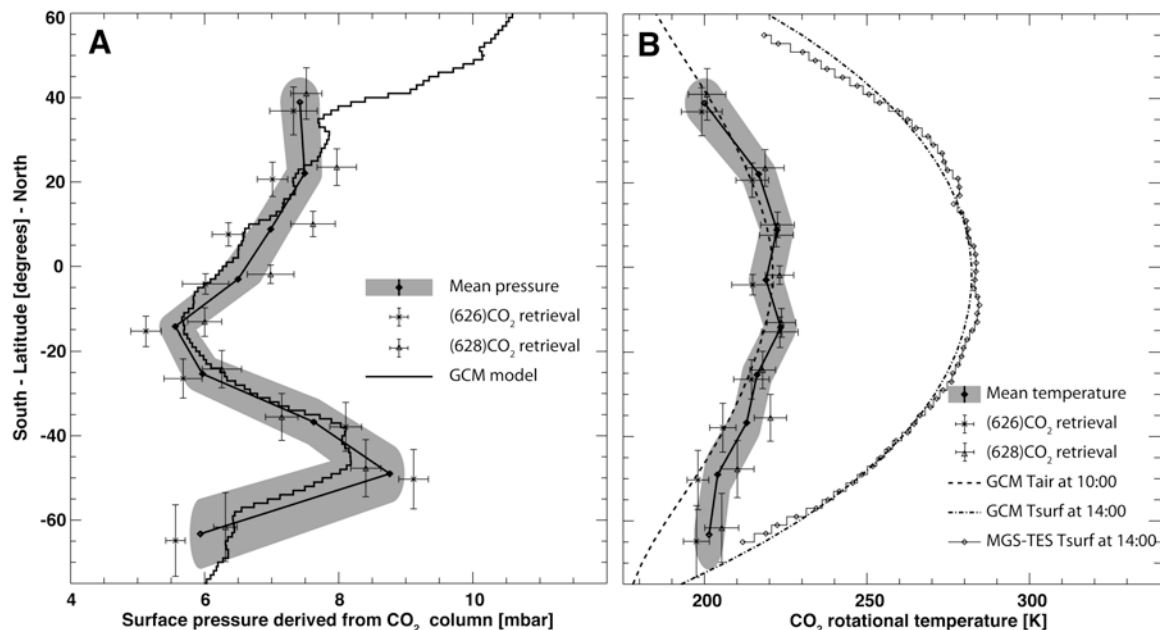
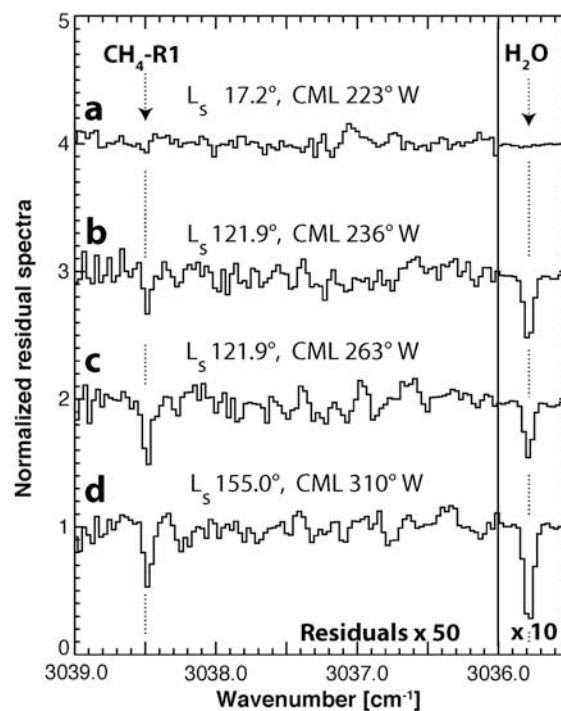


Figure S5. Retrieval of atmospheric pressure and temperature on Mars from vibrational bands of two CO₂ isotopes ($626 = {}^{16}\text{O}^{12}\text{C}^{16}\text{O}$; $628 = {}^{16}\text{O}^{12}\text{C}^{18}\text{O}$) measured with NIRSPEC at Keck-2. The spectra were taken on 16 January 2006 and the slit was oriented N-S along the central meridian longitude (CML 290° West). We retrieved the surface pressure and temperature by using a Levenberg-Marquardt non-linear-minimization algorithm and a Martian radiative transfer model. The data reveal high-temperatures at equatorial regions as predicted by the MAOAM-GCM model [16] for this season (panel B), and they sample the high atmospheric pressure of the deep Hellas basin (panel A, 42°-- S).

Figure S6. Geographic and temporal variability of methane and water on Mars. These extracts are taken from spectra centered at the indicated longitude (CML), and binned over 30 minutes in time. The sub-Earth footprints span longitude-latitude ranges with these physical dimensions: **a**: 770 km x 535 km, **b**, **c**: 1274 km x 818 km, **d**: 948 km x 586 km (Table 1). We then averaged the spectra over 5 - 50° N latitude to better reveal major changes in line intensity for methane and water vapor with location on the planet and with local season, reflecting the changing abundance ratios. Mixing ratios for methane (before latitudinal binning) are shown in Fig. 2C.



References and Notes for Supplementary material

1. A. T. Tokunaga, D. W. Toomey, J. Carr, D. N. B. Hall, H. W. Epps, in *Instrumentation in Astronomy VII*, D. Crawford, Ed., *Proc. SPIE* **1235**, part 2, 131-143 (1990).
2. T. P. Greene, A. T. Tokunaga, D. W. Toomey, J. S. Carr, In *Proc. SPIE* **1946**, 311-324 (1993).
3. I. S. McLean *et al.*, in *Infrared Astronomical Instrumentation*, A. M. Fowler, Ed., (SPIE Conf. Proc. 3354), 566 (1998).
4. G. L. Villanueva, M. J. Mumma, R. E. Novak, T. Hewagama, *Icarus* **195**, 34 (2008).
5. G. L. Villanueva, M. J. Mumma, R. E. Novak, T. Hewagama, *J. Quant. Spectrosc. Rad. Transf.* **109** (No. 6), 883 (2008).
6. D. P. Edwards, NCAR Tech. Note NCAR/TN-367+STR (1992).
7. T. Hewagama *et al.*, *Proc. SPIE* **4860**, 381 (2003).
8. T. Hewagama *et al.*, *J. Quant. Spectr. Rad. Transf.*, **109**, 1081 (2008).
9. L. S. Rothman *et al.*, *J. Quant. Spectr. Rad. Tran.* **96** (2), 139 (2005).
10. F. Forget *et al.*, *J. Geophys. Res.* **104** (E10), 24155 (1999).
11. C. B. Farmer, in *Infrared Solar Physics*, D. M. Rabin *et al.*, Eds. (IAU- Netherlands 1994), 511.
12. C. B. Farmer, R. W. Norton, in *A High Resolution Atlas of the Infrared Spectrum of the Sun and The Earth Atmosphere from Space, Vol. I: The Sun* (NASA Ref. Pub. 1224, vol. 1, Washington, DC, 1989).
13. R. E. Novak, M. J. Mumma, M. A. DiSanti, N. Dello Russo, K. Magee-Sauer, *Icarus* **158** (1), 14 (2002).
14. The Thermal Emission Spectrometer (TES) is carried on the Mars Global Surveyor spacecraft orbiting Mars (15); it provided detailed maps of H₂O, temperatures, and aerosols on Mars. We compare with updated H₂O values.
15. M. D. Smith, *Icarus* **167**, 148 (2004).
16. G. L. Villanueva, PhD thesis, Copernicus Verlag, ISBN 3-936586-34-9 (2004).
17. The Mars Observer Laser Altimeter (MOLA) is carried on the Mars Global Surveyor spacecraft orbiting Mars; it provided detailed maps of local altitudes relative to the mean geoid of Mars (18).
18. D. E. Smith *et al.*, *J. Geophys. Res.* **106** (E10), 23689 (2001).
19. A. L. Sprague *et al.*, *Icarus* **184**, 372 (2006).
20. B. M. Jakosky, R. M. Haberle, in *Mars*, H. H. Kieffer *et al.*, Eds. (Univ. Ariz. Press, Tucson, 1992).
21. B. J. Conrath *et al.*, *J. Geophys. Res.* **78**, 4267 (1973).
22. P. R. Bevington and D. K. Robinson, *Data Reduction and Error Analysis for the Physical Sciences* (McGraw-Hill, New York 1992) ISBN 0-07-911243-9.
23. F. Forget *et al.*, *J. Geophys. Res.* **112**, E08S15 (2007).
24. O. I. Korablev, V. A. Krasnopolsky, A. V. Rodin, *Icarus* **102**, 76 (1993).
25. J. Rosenqvist, E. Chassefiere, *J. Geophys. Res.* **100** (No. E3), 5541 (1995).
26. Th. Encrenaz *et al.*, *Astron. Astrophys.* **396**, 1037 (2002).
27. Mars' sidereal rotation period (at the equator) defines the sol (24.62 hr).
28. D. M. Hunten, in *Mars Atmosphere Modeling and Observations*, F. Forget *et al.*, Eds. (ESA, Noordwijk, 2006), 415.
29. S. M. Nelli *et al.*, *J. Geophys. Res.* **112**, E08S91 (August 2007).
30. A. L. Sprague *et al.*, *Science* **306**, 1364 (2004).
31. M. A. Mischna, M. I. Richardson, R. J. Wilson, D. J. McCleese, *J. Geophys. Res.* **108** (E6), 5062, 16-1 (2003).
32. W. M. Farrell, G. T. Delory, S. K. Atreya, *Geophys. Res. Lett.* **33**, L21203 (2006).
33. S. K. Atreya *et al.*, *Astrobiology* **6** (3), 439 (2006).
34. G. T. Delory *et al.*, *Astrobiology* **6** (3), 451 (2006).
35. W. C. Feldman *et al.*, *J. Geophys. Res. (Planets)* **109** (E9), IDE09006 (2004).

Endnotes for Supplementary Material:

- ¹ A. T. Tokunaga, D. W. Toomey, J. Carr, D. N. B. Hall, H. W. Epps, in *Instrumentation in Astronomy VII*, D. Crawford, Ed., *Proc. SPIE* **1235**, part 2, 131-143 (1990).
- ² T. P. Greene, A. T. Tokunaga, D. W. Toomey, J. S. Carr, In *Proc. SPIE* **1946**, 311-324 (1993).
- ³ I. S. McLean *et al.*, in *Infrared Astronomical Instrumentation*, A. M. Fowler, Ed., (SPIE Conf. Proc. 3354), 566 (1998).
- ⁴ G. L. Villanueva, M. J. Mumma, R. E. Novak, T. Hewagama, *Icarus* **195**, 34 (2008).
- ⁵ G. L. Villanueva, M. J. Mumma, R. E. Novak, T. Hewagama, *J. Quant. Spectrosc. Rad. Transf.* **109** (No. 6), 883 (2008).
- ⁶ D. P. Edwards, NCAR Tech. Note NCAR/TN-367+STR (1992).
- ⁷ T. Hewagama *et al.*, *Proc. SPIE* **4860**, 381 (2003).
- ⁸ T. Hewagama *et al.*, *J. Quant. Spectr. Rad. Transf.*, **109**, 1081 (2008).
- ⁹ L. S. Rothman *et al.*, *J. Quant. Spectr. Rad. Tran.* **96** (2), 139 (2005).
- ¹⁰ F. Forget *et al.*, *J. Geophys. Res.* **104** (E10), 24155 (1999).
- ¹¹ C. B. Farmer, in *Infrared Solar Physics*, D. M. Rabin *et al.*, Eds. (IAU- Netherlands 1994), 511.
- ¹² C. B. Farmer, R. W. Norton, in *A High Resolution Atlas of the Infrared Spectrum of the Sun and The Earth Atmosphere from Space, Vol. I: The Sun* (NASA Ref. Pub. 1224, vol. 1, Washington, DC, 1989).
- ¹³ R. E. Novak, M. J. Mumma, M. A. DiSanti, N. Dello Russo, K. Magee-Sauer, *Icarus* **158** (1), 14 (2002).
- ¹⁴ The Thermal Emission Spectrometer (TES) is carried on the Mars Global Surveyor spacecraft orbiting Mars (15); it provided detailed maps of H₂O, temperatures, and aerosols on Mars. We compare with updated H₂O values.
- ¹⁵ M. D. Smith, *Icarus* **167**, 148 (2004).
- ¹⁶ G. L. Villanueva, PhD thesis, Copernicus Verlag, ISBN 3-936586-34-9 (2004).
- ¹⁷ The Mars Observer Laser Altimeter (MOLA) is carried on the Mars Global Surveyor spacecraft orbiting Mars; it provided detailed maps of local altitudes relative to the mean geoid of Mars (18).
- ¹⁸ D. E. Smith *et al.*, *J. Geophys. Res.* **106** (E10), 23689 (2001).
- ¹⁹ A. L. Sprague *et al.*, *Icarus* **184**, 372 (2006).
- ²⁰ B. M. Jakosky, R. M. Haberle, in *Mars*, H. H. Kieffer *et al.*, Eds. (Univ. Ariz. Press, Tucson, 1992).
- ²¹ B. J. Conrath *et al.*, *J. Geophys. Res.* **78**, 4267 (1973).
- ²² P. R. Bevington and D. K. Robinson, *Data Reduction and Error Analysis for the Physical Sciences* (McGraw-Hill, New York 1992) ISBN 0-07-911243-9.
- ²³ F. Forget *et al.*, *J. Geophys. Res.* **112**, E08S15 (2007).
- ²⁴ O. I. Korablev, V. A. Krasnopolsky, A. V. Rodin, *Icarus* **102**, 76 (1993).
- ²⁵ J. Rosenqvist, E. Chassefiere, *J. Geophys. Res.* **100** (No. E3), 5541 (1995).
- ²⁶ Th. Encrenaz *et al.*, *Astron. Astrophys.* **396**, 1037 (2002).
- ²⁷ Mars' sidereal rotation period (at the equator) defines the sol (24.62 hr).
- ²⁸ D. M. Hunten, in *Mars Atmosphere Modeling and Observations*, F. Forget *et al.*, Eds. (ESA, Noordwijk, 2006), 415.
- ²⁹ S. M. Nelli *et al.*, *J. Geophys. Res.* **112**, E08S91 (August 2007).
- ³⁰ A. L. Sprague *et al.*, *Science* **306**, 1364 (2004).
- ³¹ M. A. Mischna, M. I. Richardson, R. J. Wilson, D. J. McCleese, *J. Geophys. Res.* **108** (E6), 5062, 16-1 (2003).
- ³² W. M. Farrell, G. T. Delory, S. K. Atreya, *Geophys. Res. Lett.* **33**, L21203 (2006).
- ³³ S. K. Atreya *et al.*, *Astrobiology* **6** (3), 439 (2006).
- ³⁴ G. T. Delory *et al.*, *Astrobiology* **6** (3), 451 (2006).
- ³⁵ W. C. Feldman *et al.*, *J. Geophys. Res. (Planets)* **109** (E9), IDE09006 (2004).